International Journal of
Molecular Sciences

MDPI

Article

Investigation of Structural, Morphological and Magnetic Properties of MFe_2O_4 (M = Co, Ni, Zn, Cu, Mn) Obtained by Thermal Decomposition

Thomas Dippong [1], Erika Andrea Levei [2] and Oana Cadar [2,*]

[1] Faculty of Science, Technical University of Cluj-Napoca, 76 Victoriei Street, 430122 Baia Mare, Romania; dippong.thomas@yahoo.ro
[2] INCDO-INOE 2000, Research Institute for Analytical Instrumentation, 67 Donath Street, 400293 Cluj-Napoca, Romania; erika.levei@icia.ro
* Correspondence: oana.cadar@icia.ro

Abstract: The structural, morphological and magnetic properties of MFe_2O_4 (M = Co, Ni, Zn, Cu, Mn) type ferrites produced by thermal decomposition at 700 and 1000 °C were studied. The thermal analysis revealed that the ferrites are formed at up to 350 °C. After heat treatment at 1000 °C, single-phase ferrite nanoparticles were attained, while after heat treatment at 700 °C, the $CoFe_2O_4$ was accompanied by Co_3O_4 and the $MnFe_2O_4$ by α-Fe_2O_3. The particle size of the spherical shape in the nanoscale region was confirmed by transmission electron microscopy. The specific surface area below 0.5 m^2/g suggested a non–porous structure with particle agglomeration that limits nitrogen absorption. By heat treatment at 1000 °C, superparamagnetic $CoFe_2O_4$ nanoparticles and paramagnetic $NiFe_2O_4$, $MnFe_2O_4$, $CuFe_2O_4$ and $ZnFe_2O_4$ nanoparticles were obtained.

Keywords: ferrite; thermal decomposition; heating temperature; crystalline phase; specific surface; magnetic behavior

check for updates

Citation: Dippong, T.; Levei, E.A.; Cadar, O. Investigation of Structural, Morphological and Magnetic Properties of MFe_2O_4 (M = Co, Ni, Zn, Cu, Mn) Obtained by Thermal Decomposition. *Int. J. Mol. Sci.* **2022**, *23*, 8483. https://doi.org/10.3390/ijms23158483

Academic Editor: Daniel Arcos

Received: 11 July 2022
Accepted: 28 July 2022
Published: 30 July 2022

Publisher's Note: MDPI stays neutral with regard to jurisdictional claims in published maps and institutional affiliations.

Copyright: © 2022 by the authors. Licensee MDPI, Basel, Switzerland. This article is an open access article distributed under the terms and conditions of the Creative Commons Attribution (CC BY) license (https://creativecommons.org/licenses/by/4.0/).

1. Introduction

Spinel ferrites of MFe_2O_4 (M = Co, Ni, Zn, Cu, Mn) type have a cubic, closely packed arrangement of oxygen atoms with M^{2+} and Fe^{3+} ions occupying the tetrahedral (A) and octahedral (B) sites [1]. The spinel structure determines excellent magnetic and electrical properties, high chemical stability and low production costs [1–10]. These interesting properties enable the use of nanostructured materials in a wide range of novel applications in the field of science and technology [9–13].

Cobalt ferrite ($CoFe_2O_4$), nickel ferrite ($NiFe_2O_4$) and copper ferrite ($CuFe_2O_4$) have inverse spinel structures with M^{2+} (M^{2+} = Co^{2+}, Ni^{2+} or Cu^{2+}) ions occupying the octahedral (B) sites and Fe^{3+} ions equally distributed between the tetrahedral (A) and octahedral (B) sites [5,14]. Zinc ferrite ($ZnFe_2O_4$) has a normal spinel ferrite with Zn^{2+} ions in tetrahedral (A) and Fe^{3+} ions in octahedral (B) sites, while manganese ferrite ($MnFe_2O_4$) has a partially inverse spinel structure, in which only 20% of divalent Mn^{2+} ions are located at octahedral (B) sites and the remainder of them are positioned at tetrahedral (A) sites [6].

$CoFe_2O_4$ is a ferromagnetic material with unique characteristics, such as large coercivity, magnetocrystalline anisotropy, Curie temperature and electrical resistance, remarkable thermal stability, moderate saturation magnetization, good chemical and mechanical stability, low eddy current loss and production cost [2,3,11,15]. These properties make it a promising candidate for various kind of applications such as drug delivery, magnetic resonance imaging, magnetic storage devices, catalysts and adsorption of toxic metals [15–19]. $CoFe_2O_4$ with unique architectures, including nanoparticles, hollow nanospheres, mesoporous nanospheres, nanorods and three-dimensional ordered macroporous structures, have been produced in the last years [3].

$NiFe_2O_4$ may display paramagnetic, superparamagnetic or ferrimagnetic behavior depending on the particle size and shape [20]. Due to its high magnetocrystalline anisotropy, high-saturation magnetization and unique magnetic structure combined with high Curie temperature, low coercivity, low eddy current loss, low price and high electrochemical stability [12,20–22] it is one of the most suitable candidates for applications in biosensors, corrosion protection, drug delivery, ceramics, medical diagnostics, microwave absorbers, transformer cores, magnetic liquids, magnetic refrigeration and high-density magnetic recording media, water-oxidation processes, dye removal by magnetic separation, etc. [5,21–23].

$CuFe_2O_4$ is a soft material with low coercivity, low-saturation magnetization, high electrical resistance, low eddy current losses, great resistance to corrosion, thermal stability, excellent catalytic properties and environmental benignity, and it is not readily demagnetized [12,14,24,25]. $CuFe_2O_4$ shows ferromagnetic behavior with a single-domain state and is widely used in magnetic storage, catalysis, photocatalysis, pollutant removal from wastewater, color imaging, magnetic refrigeration, magnetic drug delivery and high-density information storage [8,12,24–26].

$ZnFe_2O_4$ possess exceptional structural, optical, magnetic, electrical and dielectric properties at nanoscale, besides low toxicity, chemical and thermal stability [5,7,9,11,15]. $ZnFe_2O_4$ is antiferromagnetic at temperatures below the Neel temperature, but when the size of $ZnFe_2O_4$ approaches the nanometer range, it transforms into a diamagnetic, superparamagnetic or ferromagnetic substance [12,18]. Consequently, it has a wide potential to be used in microwave absorption, energy storage, drug delivery, magnetic resonance imaging, gas sensors, absorbent material for hot-gas desulphurization, high-performance electrode materials, photocatalysts and pigments [5,9,11,12,27]. Additionally, $ZnFe_2O_4$ is a promising semiconductor that can sensitize and activate under visible light other photocatalysts due to its small band gap [28].

$MnFe_2O_4$ have controllable grain size, high magnetization value, superparamagnetic nature, ability to be monitored by an external magnetic field, an easy synthesis process, surface manipulation ability, greater biocompatibility, thermal stability, non–toxicity, non-corrosion and environmentally friendly ability. Its properties have attracted potential consideration in biomedicine, in ceramic and paint industry as black pigment, and in high-frequency magnetostrictive and electromagnetic applications [6,29,30].

Synthesis methods with low toxicity that are also economical in terms of energy consumption, allowing for the production of fine, nanosized, highly pure, single-phase nanocrystalline ferrites have received considerable interest [31]. Spinel ferrites are commonly synthesized using the ceramic technique, which infers high temperatures and produces particles with small specific surface. In order to achieve ferrites with large specific surface and high degree of homogeneity, different synthesis methods, namely coprecipitation, polymeric gel, hydrothermal, microemulsion, heterogeneous precipitation, sonochemistry, combustion, sol–gel methods, etc. were used [31]. Despite the resulting fine-grained microstructure, the chemical methods have some disadvantages such as necessity of complex apparatus, long reaction time and post–synthesis thermal treatment to complete the formation and crystallization of final products, poor crystallinity and broad particle size distribution, which may negatively influence the related properties (shape, surface area and porosity) [32]. The sol–gel method has been used to prepare fine, homogenous, highly dense and single-phase ferrite nanoparticles. Compared to other conventional methods, the sol–gel method provides a good stoichiometric control and produces ferrites at relatively low temperatures. Furthermore, it allows for the embedding of ferrites into silica (SiO_2) matrix to prevent particle growth and particle agglomeration and to improve the magnetic properties [16,33]. However, despite its noticeable advantages, its main disadvantage consists of limited efficiency and long processing time [34]. The thermal decomposition method is a very efficient synthesis strategy, based on the heating of metallic precursors at different temperatures. Additionally, this method is simple and environmentally friendly,

has a relatively low cost, requires a low reaction temperature and provides small particle size, narrow size distribution and no toxic by-products [35].

This paper focuses on the structural and morphological characteristics as well as the magnetic properties of nanosized $CoFe_2O_4$, $NiFe_2O_4$, $ZnFe_2O_4$, $CuFe_2O_4$ and $MnFe_2O_4$, obtained by thermal decomposition at 700 and 1000 °C. To the best of our knowledge, this is the first work that investigates the structural, morphological and magnetic properties of nanoferrites obtained by thermal decomposition of nitrates and compares them with those of correspondent nanoferrites embedded in SiO_2 matrix obtained by sol–gel method. The reaction progress was monitored by thermal (TG/DTA) analysis, while the nanoferrite composition was investigated by inductively coupled plasma optical emission spectrometry (ICP-OES). The crystalline phases and crystallite size were investigated by X-ray diffraction (XRD), while the particle properties such as shape, size and agglomeration were studied by transmission electron microscopy (TEM). The influence of crystallite size and divalent ions on the magnetic properties and the variation of saturation magnetization, remanent magnetization, coercivity and anisotropy of nanoferrites were also studied.

2. Results

Figure 1 presents the thermal decomposition diagrams (thermogravimetric—TG and differential thermal—DTA) of MFe_2O_4 systems. On the DTA diagram, the formation of $CoFe_2O_4$ is indicated by three endothermic effects at 63, 143 and 195 °C and two exothermic effects at 253 and 303 °C, respectively. The total mass loss is 65%. $NiFe_2O_4$, $ZnFe_2O_4$ and $CuFe_2O_4$ show two endothermic effects at 96 and 210 °C, 69 and 213 °C, 83 and 204 °C and an exothermic effect at 279, 267 and 289 °C, respectively. The total mass loss is 63% for $NiFe_2O_4$, 57% for $ZnFe_2O_4$ and 62% for $CuFe_2O_4$, respectively. The formation of $MnFe_2O_4$ is showed by three endothermic effects at 69, 132 and 201 °C, and an exothermic effect at 270 °C. The total mass loss shown on the TG diagram is 60%.

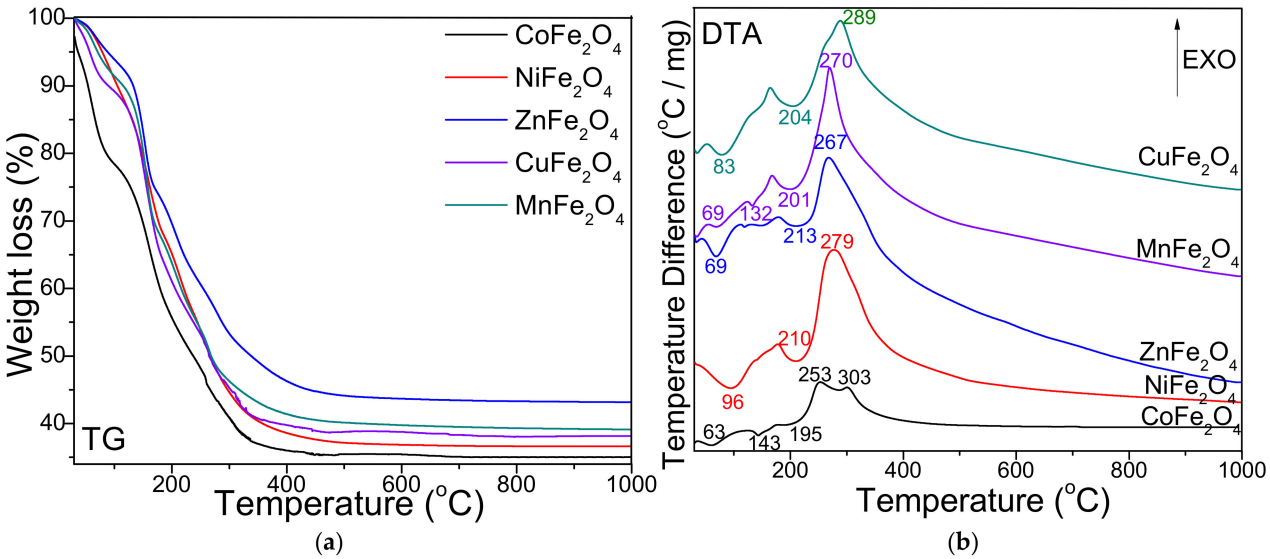


Figure 1. Thermogravimetric (TG) (**a**) and differential thermal analysis (DTA) (**b**) diagrams for MFe_2O_4 (M = Co, Ni, Zn, Cu, Mn).

The crystalline phases after heat treatment at 700 and 1000 °C are presented in Figure 2. The XRD pattern of $CoFe_2O_4$ exhibits a single-phase cubic spinel $CoFe_2O_4$ (JCPDS card no. 22-1086, [36]), belonging to *Fd3m* space group at 1000 °C, while at 700 °C, the presence of Co_3O_4 (JCPDS card no. 80-1451 [36]) is also remarked. In case of $NiFe_2O_4$, $ZnFe_2O_4$ and $CuFe_2O_4$ at both temperatures, single phase crystalline $NiFe_2O_4$ (JCPDS card no. 89-4927 [36]), $ZnFe_2O_4$ (JCPDS card no. 16-6205 [36]) and $CuFe_2O_4$ (JCPDS card no. 25-0283 [36]) are remarked. The presence of ZnO or CuO identified in case of ferrites embedded in SiO_2 matrix was not observed [33]. Single-phase crystalline $MnFe_2O_4$ (JCPDS card no.

74-2403 [36]) is obtained at 1000 °C, while at 700 °C, the $MnFe_2O_4$ is accompanied by α-Fe_2O_3 (JCPDS card no. 87-1164 [36]).

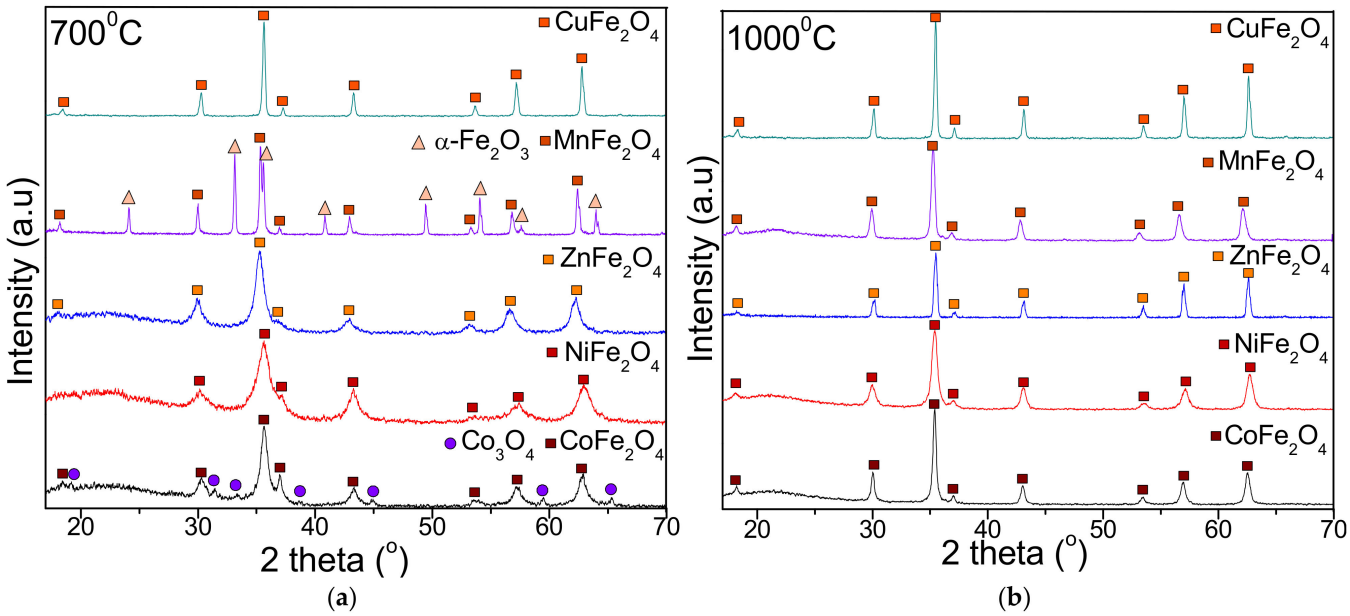


Figure 2. X-ray diffraction pattern of MFe_2O_4 (M = Co, Ni, Zn, Mn, Cu) heat treated at 700 °C (**a**) and 1000 °C (**b**).

The average crystallite size was estimated using the most intense diffraction (311) peak from the Debye–Scherrer formula [7,23,25] (Table 1). The crystallite size increases with the heating temperature, with the largest crystallite size being observed for $CuFe_2O_4$ at 1000 °C (81 nm), while the smallest crystallite size was observed for $ZnFe_2O_4$ at 700 °C (13 nm). The lattice parameter (a) also increases with the annealing temperature, with the highest value being observed for $NiFe_2O_4$ at 1000 °C (8.365 Å), while the lowest value observed was for $CuFe_2O_4$ at 700 °C (8.207 Å). The M/Fe molar ratio calculated based on Co, Mn, Zn, Ni and Fe concentrations measured by ICP-OES confirms the theoretical elemental composition of the obtained nanoferrites (Table 1). In all cases, the best fit of experimental and theoretical data is remarked for samples annealed at 1000 °C. In case of $CoFe_2O_4$ and $MnFe_2O_4$ annealed at 700 °C, the M/Fe molar ratio could not be calculated due to the presence of Co_3O_4 and α-Fe_2O_3 as secondary phases.

Table 1. Average particle size (D_{PS}), average crystallite size (D_{CS}), lattice parameter (a) and M/Fe molar ratio for MFe_2O_4 (M = Co, Ni, Zn, Mn, Cu) heat treated at 700 and 1000 °C.

	Temperature (°C)	$CoFe_2O_4$	$NiFe_2O_4$	$ZnFe_2O_4$	$MnFe_2O_4$	$CuFe_2O_4$
D_{PS} (nm)	1000	78	52	68	32	85
D_{CS} (nm)	700	23	18	13	14	27
	1000	69	49	57	29	81
a (Å)	700	8.275	8.258	8.278	8.269	8.207
	1000	8.334	8.365	8.342	8.318	8.302
M/Fe molar ratio	700	-	0.98/2.04	0.97/2.01	-	0.98/2.03
	1000	0.99/2.00	0.99/2.01	0.99/2.00	0.98/1.99	1.00/2.01

Due to the low amount of adsorbed/desorbed nitrogen, the determination of porosity and specific surface area (SSA) for samples heat treated at 700 and 1000 °C was not possible. The SSA below the method detection limit (0.5 m^2/g), suggests that all ferrites have a

non–porous structure, probably as a consequence of particle agglomeration that limits the absorption of nitrogen.

According to TEM images, the nanoparticles have spherical shape. The particle sizes estimated by XRD and TEM are comparable, the low differences appearing probably due to some large-size nanoparticles. $CuFe_2O_4$ displays the largest particle size (85 nm), while $MnFe_2O_4$ has the smallest particle size (32 nm) (Table 1 and Figure 3).

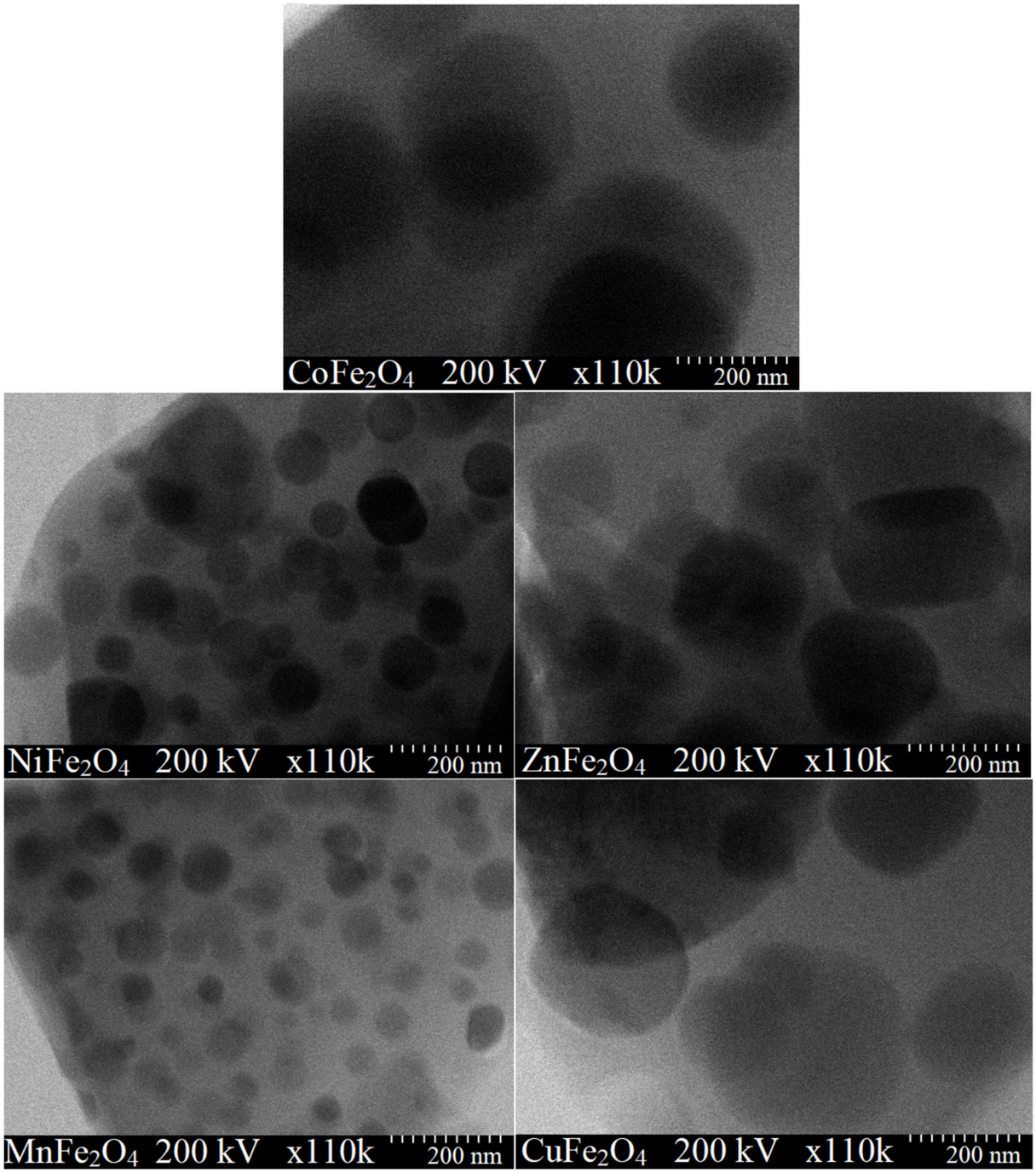


Figure 3. TEM images for MFe_2O_4 (M = Co, Zn, Ni, Cu, Mn) heat treated at 1000 °C.

The hysteresis loops (Figure 4) have an S-shape at low magnetic fields and are linear at higher fields, indicating the presence of small-sized magnetic particles with superparamagnetic behavior [37]. The spin rotation energy for particles smaller than the critical diameter is lower than the thermal energy. Thus, in the absence of an applied magnetic field, the

random orientation of the magnetic moments results in zero average global magnetic moment [36].

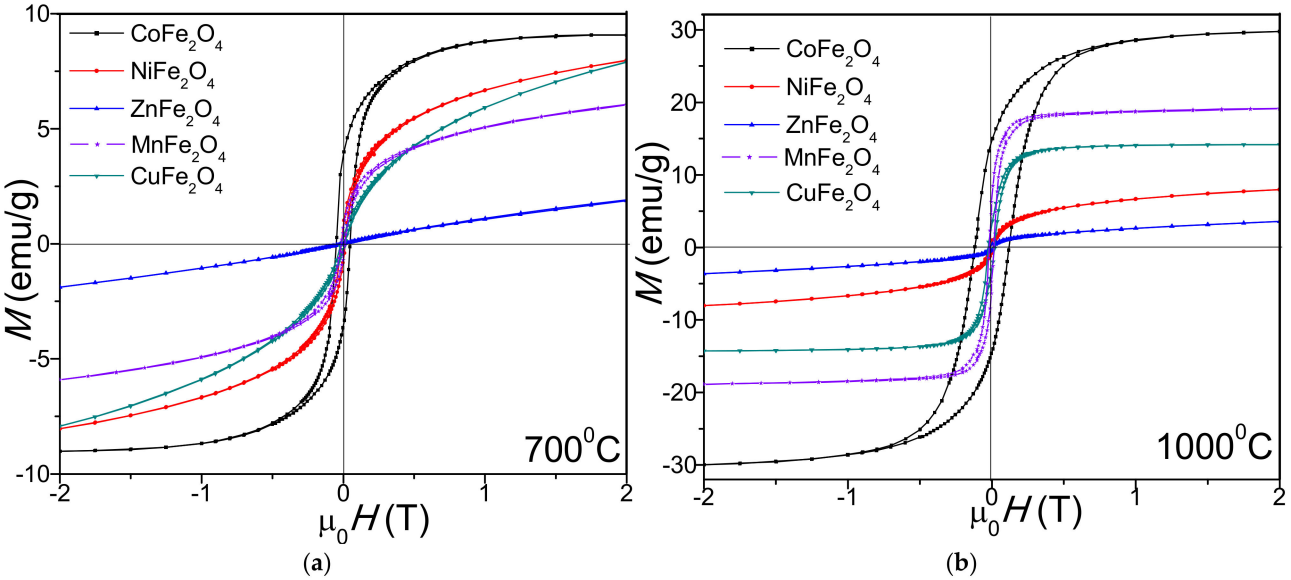


Figure 4. Magnetic hysteresis loops of MFe_2O_4 (M = Co, Zn, Ni, Cu, Mn) heat treated at 700 °C (**a**) and 1000 °C (**b**).

The saturation magnetization (M_S) and remanent magnetization (M_R) increase with the increase of heating temperature, with the highest values being measured for $CoFe_2O_4$ (29.7 emu/g) and the lowest for $ZnFe_2O_4$ (2.45 emu/g), as shown in Table 2. The coercivity (H_C) increases (from 49.5 Oe to 131 Oe in case of $CoFe_2O_4$) with the increase of heating temperature, indicating that the magnetic moment arrangement is highly disordered at high heating temperatures [27].

Table 2. Saturation magnetization (M_S), remanent magnetization (M_R), coercivity (H_C), squareness (S) and magnetic anisotropy constant (K) of MFe_2O_4 (M = Co, Zn, Ni, Cu, Mn) heat treated at 700 and 1000 °C.

	Temperature (°C)	$CoFe_2O_4$	$NiFe_2O_4$	$ZnFe_2O_4$	$CuFe_2O_4$	$MnFe_2O_4$
M_S (emu/g)	700	9.20	8.08	1.89	7.91	6.08
	1000	29.7	11.2	2.45	14.2	19.1
M_R (emu/g)	700	3.98	1.55	0.142	1.11	0.98
	1000	14.1	8.14	0.695	9.82	1.55
H_C (Oe)	700	49.5	4.62	1.81	10.4	20.8
	1000	131	12.8	10.1	14.7	51.6
S	700	0.437	0.192	0.075	0.143	0.161
	1000	0.475	0.727	0.284	0.692	0.081
K × 10^3 (erg/cm^3)	700	0.286	0.023	0.002	0.052	0.079
	1000	2.44	0.090	0.015	0.131	0.619

In all cases, the squareness ratio (S, 0.075 for $ZnFe_2O_4$ at 700 °C—0.727 for $NiFe_2O_4$ at 1000 °C), the anisotropy constant (K, 0.002 × 10^3 erg/cm^3 for $ZnFe_2O_4$ at 700 °C—2.44 × 10^3 erg/cm^3 for $CoFe_2O_4$ at 1000 °C) also increase with the increase of heating temperature. Compared to the same ferrites embedded in SiO_2 matrix, the K value is much lower [33].

3. Discussion

The thermal behavior of $Fe^{III}(NO_3)_3$–$M^{II}(NO_3)_2$–1,3-propanediol solutions was studied by DTA. The endothermic effect at 70–100 °C is attributed to the loss of moisture and of crystallization water from the metallic nitrates used in the synthesis. The endothermic effect at 132–213 °C on the DTA diagram is attributed to formation of metal-malonate precursor. The formation of metal-malonate precursor for $CoFe_2O_4$ and $ZnFe_2O_4$ takes place in two stages as indicated by the two endothermic effects. The first endothermic effect was assigned to the divalent metal-malonate formation (143 °C for Co-malonate and 132 °C for Mn-malonate), while the second endothermic effect (around 201 °C) was assigned to the formation of Fe-malonate. In case of the other synthesis, the divalent metal (Ni, Zn, Cu) malonates and the trivalent Fe-malonate formation takes place in a single stage (204–213 °C). The formation of ferrites by decomposition of malonate precursors is indicated on the DTA diagram by a single exothermic effect at 250–350 °C, except for $CoFe_2O_4$, where two exothermic effects appear at 253 and 303 °C. The two-stage formation of $CoFe_2O_4$ in the metal nitrates–diol mixture could be explained by the fact that the aqua cation $[Fe(H_2O)_6]^{3+}$ is a stronger acid than the aqua cation $[Co(H_2O)_6]^{2+}$ [17,36]. The highest mass loss shown on the TG diagram is attributed to $CoFe_2O_4$ (65%), while the lowest mass loss is attributed to $ZnFe_2O_4$ (57%), probably due to the fact that $ZnFe_2O_4$ is quantitatively obtained at lower temperatures compared to other ferrites accompanied by other crystalline or amorphous secondary phases.

The increase of heating temperature from 700 to 1000 °C did not affect the crystal structure of the studied ferrites but improved the phase purity [10]. Moreover, by increasing the heating temperature, the diffraction peaks become sharper and narrower, indicating the formation of larger particles due to grain growth [25,38]. After heat treatment at 1000 °C, an important agglomeration of the particles takes place without consequent recrystallization, supporting the formation of single crystals rather than polycrystals [1,2,6]. Oppositely, at 700 °C, the surface dipole–dipole interactions, high surface energy and tension, as well as the change of cation distribution within the nanocrystallite, induces lattice shrinking, which further inhibits grain growth [1–6]. Generally, the size of the crystallite is higher than the size of the corresponding ferrites embedded in SiO_2 matrix, produced by sol–gel method [15–19]. These findings indicate that the heating temperature and the synthesis route plays a key role in determining the crystallite size [8]. Crystallite size has a significant effect on the magnetic and optical properties of the material, especially when the grain size is approaching the crystallite size [4–6,38].

The different particle size of the produced ferrites may be attributed to different kinetics of metal oxides formation, different particle growth rate or presence of structural disorder and strain in the lattice caused by different ionic radii [39] The different particle arrangement is attributed to the formation of well-delimited particles that generate solid boundaries. Moreover, interfacial surface tensions appear most likely due to the agglomeration tendency of small particles, weak surface interaction due to Van der Waals forces and magnetic interactions [39].

The magnetic properties of nanoferrites are strongly influenced by the cation distribution between the tetrahedral (A) and octahedral (B) sites, as well as by the interactions between the magnetic ions [37,40]. Different size and morphology of the nanoparticles at different heating temperatures results in different surface spin disorder, pinned magnetic moment, different surface spin canting and consequently different cation inversion in the spinel structure and magnetic features [8]. The lower M_S values of ferrites heat treated at 700 °C compared to those at 1000 °C result from the lower crystallinity at 700 °C, presence of vacancies, interatomic spacing, low coordination number and surface spin disorder [37].

At 1000 °C, the $CoFe_2O_4$ has superparamagnetic behavior, while the other ferrites display paramagnetic behavior. The superparamagnetic behavior is attributed to the high disorder of the magnetic moment orientation with the increase in the surface-area-to-volume ratio [41]. For $MnFe_2O_4$, the sharp increase in M_S with the increase of heating temperature could be explained by the formation of trace paramagnetic α-Fe_2O_3 [27,30].

The $ZnFe_2O_4$ heat treated at 700 °C is paramagnetic, the low M_S values being attributed to the lattice defects, core–shell interactions, spin canting, disordered cation distribution, A–B super exchange interaction and random spin orientation on the surface of nanoparticles [30]. The M_S values reported for $ZnFe_2O_4$ differ from study to study, indicating that M_S strongly depends on the synthesis route and heating temperature [27,41]. The changes of $CuFe_2O_4$ magnetic properties following the reduction in bulk grain size of $CuFe_2O_4$ nanoparticles by milling was reported by Soufi et al. [12]. The M_S value of $NiFe_2O_4$ is lower than that of $MnFe_2O_4$ and $CoFe_2O_4$, probably due to the increase in surface effects with the decrease in particle size [20]. The influences of surface effect on the magnetic properties may be explained by the different exchange interactions and presence of magnetic defects on the nanoparticles surface [20]. Priyadharsini et al. also reported the M_S, M_R and H_C values increasing with the heating temperature [25].

Generally, the H_C of the spinel ferrite nanoparticles is governed by the magnetocrystalline anisotropy, strain, interparticle interaction, grain size and morphology [42]. The H_C also increase with the increase in the surface potential barrier caused by crystalline lattice defects such as the deviation of atoms from the normal positions in the surface layers [43]. The influence of the particle sizes, internal strain, magnetic domain structure, shape and magnetocrystalline anisotropy of the nanoparticles on the H_C value is not fully explained [43]. The low H_C of all ferrites for both heating temperatures indicate an enhanced coalescence of the crystallites that further results in strong magnetic coupling and high magnetization [43]. At both temperatures, the H_C of $CoFe_2O_4$ nanoparticles prepared by thermal decomposition increases with the particle-size increase, suggesting the presence of a single magnetic domain [8]. The transition from superparamagnetic to ferromagnetic behavior of $CoFe_2O_4$ was noticed after heat treatment at 1000 °C [25]. The different H_C of $NiFe_2O_4$ is attributed both to the crystallite size and the presence of shape anisotropy [30].

The increasing squareness ratio (S) at high heating temperatures could be the consequence of the reorientation of grains along the easy axis of magnetization when the field is switched off [25]. The main factors that influence the magnetic anisotropy are the crystallographic directions, surface defects and irregularities [44,45]. The high H_C and K of $CoFe_2O_4$ are the consequence of Co^{2+} ions in octahedral (B) sites, which induce frozen orbital angular momentum and strong spin-orbital coupling [8,46].

4. Materials and Methods

$Fe(NO_3)_3 \cdot 9H_2O$, $Co(NO_3)_2 \cdot 6H_2O$, $Ni(NO_3)_2 \cdot 6H_2O$, $Zn(NO_3)_2 \cdot 6H_2O$, $Cu(NO_3)_2 \cdot 3H_2O$, $Mn(NO_3)_2 \cdot 3H_2O$ and 1,3-propanediol of purity higher than 98% were purchased from Merck (Darmstadt, Germany) and used as received.

MFe_2O_4 (M = Co, Zn, Ni, Cu, Mn) were synthesized by mixing the metal nitrates in 1M/2Fe molar ratio with 1,3-propanediol in equimolecular ratio of NO_3^-/1,3-propanediol. The resulted solutions were heat treated at 700, and 1000 °C (5 h) in air using a LT9 muffle furnace (Nabertherm, Lilienthal, Germany).

The ferrite formation was investigated by thermogravimetry (TG) and differential thermal analysis (DTA) using a Q600 SDT (TA Instruments, New Castle, DE, USA) analyzer, in air, up to 1000 °C, at 10 °C·min^{-1} using alumina standards. The crystalline phases were investigated by X-ray diffraction using a D8 Advance (Bruker, Karlsruhe, Germany), at ambient temperature, with CuKα radiation (λ = 1.54060 Å) and LynxEye detector, operating at 40 kV and 40 mA. The Co/Fe ($CoFe_2O_4$), Ni/Fe ($NiFe_2O_4$), Zn/Fe ($ZnFe_2O_4$), Cu/Fe ($CuFe_2O_4$) and Mn/Fe ($MnFe_2O_4$) molar ratios were confirmed using an Optima 5300 DV (Perkin Elmer, Norwalk, CT, USA) inductively coupled plasma optical emission spectrometer (ICP-OES), spectrometer, after microwave digestion (Xpert microwave system, Berghof, Eningen, Germany) with aqua regia. Specific surface area (SSA) was calculated using the BET model from N_2 adsorption–desorption isotherms recorded at 196 °C on samples degassed for 4 h at 150 °C and 2 Pa pressure using a Sorptomatic 1990 (Thermo Fisher Scientific, Waltham, MA, USA) instrument. The shape and clustering of nanoparticles were studied on samples deposited and dried on carbon-coated copper grids

using a transmission electron microscope (TEM, HD-2700, Hitachi, Tokyo, Japan). The magnetic measurements were performed using a 7400 vibrating-sample magnetometer (VSM, LakeShore Cryotronics, Westerville, OH, USA). The hysteresis loops were recorded at room temperature in magnetic fields between −2 to 2 Tesla.

5. Conclusions

The structural, morphological and magnetic characteristics of nanosized $CoFe_2O_4$, $NiFe_2O_4$, $ZnFe_2O_4$, $CuFe_2O_4$ and $MnFe_2O_4$ obtained by thermal decomposition were investigated. The formation of ferrites appeared as a single exothermic effect at 250–350 °C, excepting $CoFe_2O_4$ with two exothermic effects. The highest mass loss was attributed to $CoFe_2O_4$ (65%), while the lowest mass loss was assigned to $ZnFe_2O_4$ (55%). Unlike similar ferrites embedded in SiO_2 matrix, at both temperatures, single crystalline phases were remarked, excepting the presence of Co_3O_4 (in case of $CoFe_2O_4$) and α-Fe_2O_3 (in case of $MnFe_2O_4$) at 700 °C. The SSA values lower than 0.5 m^2/g indicated a non–porous structure due to the particle agglomeration. $CuFe_2O_4$ showed the largest particle size (85 nm), while $MnFe_2O_4$ had the smallest particle size (32 nm). The crystalline $CoFe_2O_4$ heat treated at 1000 °C displayed the highest Ms, H_C and K values, presenting superparamagnetic behavior, while the other ferrites exhibited paramagnetic behavior.

Author Contributions: Conceptualization, methodology, investigation, writing—original draft, visualization, supervision, T.D.; methodology, investigation, writing—review, E.A.L. and O.C. All authors have read and agreed to the published version of the manuscript.

Funding: The APC was funded by Technical University of Cluj-Napoca Grant Support GC1/2021.

Institutional Review Board Statement: Not applicable.

Informed Consent Statement: Not applicable.

Data Availability Statement: Not applicable.

Acknowledgments: This study was supported by the Ministry of Research, Innovation and Digitization through Program 1—Development of the national research & development system, Subprogram 1.2—Institutional performance—Projects that finance the RDI excellence, Contract no. 18PFE/30 December 2021.

Conflicts of Interest: The authors declare no conflict of interest. The funders had no role in the design of the study; in the collection, analyses, or interpretation of data; in the writing of the manuscript; or in the decision to publish the results.

References

1. Mylarappa, M.; Lakshmi Venkata, V.; Mahesh Vishnu, K.R.; Raghavendra, N.; Nagaswarupa, H.P. Cyclic voltammetry, impedance and thermal properties of $CoFe_2O_4$ obtained from waste Li-Ion batteries. *Mater. Today Proc.* **2018**, *5*, 22425–22432. [CrossRef]
2. Xiong, Q.Q.; Tu, J.P.; Shi, S.J.; Liu, X.J.; Wang, X.L.; Gu, C.D. Ascorbic acid-assisted synthesis of cobalt ferrite ($CoFe_2O_4$) hierarchical flower-like microspheres with enhanced lithium storage properties. *J. Power Sources* **2014**, *256*, 153–159. [CrossRef]
3. Shetty, K.; Renuka, L.; Nagaswarupa, H.P.; Nagabhushana, H.; Anantharaju, K.S.; Rangappa, D.; Prashantha, S.C.; Ashwini, K. A comparative study on $CuFe_2O_4$, $ZnFe_2O_4$ and $NiFe_2O_4$: Morphology, impedance and photocatalytic studies. *Mater. Today Proc.* **2017**, *4*, 11806–11815. [CrossRef]
4. Asghar, K.; Qasim, M.; Das, D. Preparation and characterization of mesoporous magnetic $MnFe_2O_4$@$mSiO_2$ nanocomposite for drug delivery application. *Mater. Today Proc.* **2020**, *26*, 87–93. [CrossRef]
5. Chand, P.; Vaish, S.; Kumar, P. Structural, optical and dielectric properties of transition metal (MFe_2O_4; M = Co, Ni and Zn) nanoferrites. *Phys. B* **2017**, *524*, 53–63. [CrossRef]
6. Revathi, J.; Abel, M.J.; Archana, V.; Sumithra, T.; Thiruneelakandan, R. Synthesis and characterization of $CoFe_2O_4$ and Ni-doped $CoFe_2O_4$ nanoparticles by chemical Co-precipitation technique for photo-degradation of organic dyestuffs under direct sunlight. *Phys. B* **2020**, *587*, 412136. [CrossRef]
7. Li, X.; Sun, Y.; Zong, Y.; Wei, Y.; Liu, X.; Li, X.; Peng, Y.; Zheng, X. Size-effect induced cation redistribution on the magnetic properties of well-dispersed $CoFe_2O_4$ nanocrystals. *J. Alloy. Compd.* **2020**, *841*, 155710. [CrossRef]
8. Shilpa Amulya, M.A.; Nagaswarupta, H.P.; Anil Kumar, M.R.; Ravikumar, C.R.; Kusuma, K.B.; Prashantha, S.C. Evaluation of bifunctional applications of $CuFe_2O_4$ nanoparticles synthesized by a sonochemical method. *J. Phys. Chem. Solids* **2021**, *148*, 109756. [CrossRef]

9. Peng, S.; Wang, S.; Liu, R.; Wu, J. Controlled oxygen vacancies of $ZnFe_2O_4$ with superior gas sensing properties prepared via a facile one-step self-catalyzed treatment. *Sens. Actuators B Chem.* **2019**, *288*, 649–655. [CrossRef]
10. Cui, K.; Sun, M.; Zhang, J.; Xu, J.; Zhai, Z.; Gong, T.; Hou, L.; Yuan, C. Facile solid-state synthesis of tetragonal $CuFe_2O_4$ spinels with improved infrared radiation performance. *Ceram. Int.* **2022**, *48*, 10555–10561. [CrossRef]
11. Sarkar, K.; Mondal, R.; Dey, S.; Kumar, S. Cation vacancy and magnetic properties of $ZnFe_2O_4$ microspheres. *Phys. B Condens. Matter* **2020**, *583*, 412015. [CrossRef]
12. Soufi, A.; Hajjaoui, H.; Elmoubarki, R.; Abdennouri, M.; Qourzal, S.; Barka, N. Heterogeneous Fenton-like degradation of tartrazine using $CuFe_2O_4$ nanoparticles synthesized by sol-gel combustion. *Appl. Surf. Sci. Adv.* **2022**, *9*, 100251. [CrossRef]
13. Rajini, R.; Ferdinand, A.C. Structural, morphological and magnetic properties of (c-$ZnFe_2O_4$ and t-$CuFe_2O_4$) ferrite nanoparticle synthesized by reactive ball milling. *Chem. Data Collect.* **2022**, *38*, 100825. [CrossRef]
14. Iqbal, M.J.; Yaqub, N.; Sepiol, B.; Ismail, B. A study of the influence of crystallite size on the electrical and magnetic properties of $CuFe_2O_4$. *Mater. Res. Bull.* **2011**, *46*, 1837–1842. [CrossRef]
15. Dey, A.; Saini, B. Effect of various surfactant templates on the physicochemical properties of $CoFe_2O_4$ nanoparticles. *Mater. Today Proc.* **2022**, *61*, 351–355. [CrossRef]
16. Dippong, T.; Levei, E.A.; Lengauer, C.L.; Daniel, A.; Toloman, D.; Cadar, O. Investigation of thermal, structural, morphological and photocatalytic properties of $Cu_xCo_{1-x}Fe_2O_4$ ($0 \leq x \leq 1$) nanoparticles embedded in SiO_2 matrix. *Mater. Charact.* **2020**, *163*, 110268. [CrossRef]
17. Stefanescu, M.; Dippong, T.; Stoia, M.; Stefanescu, O. Study on the obtaining of cobalt oxides by thermal decomposition of some complex combinations, undispersed and dispersed in SiO_2 matrix. *J. Therm. Anal. Calorim.* **2008**, *94*, 389–393. [CrossRef]
18. Dippong, T.; Levei, E.A.; Goga, F.; Petean, I.; Avram, A.; Cadar, O. The impact of polyol structure on the formation of $Zn_{0.6}Co_{0.4}Fe_2O_4$ spinel-based pigments. *J. Sol-Gel Sci. Technol.* **2019**, *93*, 736–744. [CrossRef]
19. Dippong, T.; Levei, E.A.; Cadar, O.; Mesaros, A.; Borodi, G. Sol-gel synthesis of $CoFe_2O_4$: SiO_2 nanocomposites–insights into the thermal decomposition process of precursors. *J. Anal. Appl. Pyrolysis* **2017**, *125*, 169–177. [CrossRef]
20. Sivakumar, A.; Dhas, S.S.J.; Dhas, S.A.M.B. Assessment of crystallographic and magnetic phase stabilities on $MnFe_2O_4$ nano crystalline materials at shocked conditions. *Solid State Sci.* **2020**, *107*, 106340. [CrossRef]
21. Ozçelik, B.; Ozçelik, S.; Amaveda, H.; Santos, H.; Borrell, C.J.; Saez-Puche, R.; de la Fuente, G.F.; Angurel, L.A. High speed processing of $NiFe_2O_4$ spinel using laser furnance. *J. Mater.* **2020**, *6*, 661–670.
22. Hoghoghifard, S.; Moradi, M. Influence of annealing temperature on structural, magnetic, and dielectric properties of $NiFe_2O_4$ nanorods synthesized by simple hydrothermal method. *Ceram. Int.* **2022**, *48*, 17768–17775. [CrossRef]
23. Majid, F.; Rauf, J.; Ata, S.; Bibi, I.; Malik, A.; Ibrahim, S.M.; Ali, A.; Iqbal, M. Synthesis and characterization of $NiFe_2O_4$ ferrite: Sol–gel and hydrothermal synthesis routes effect on magnetic, structural and dielectric characteristics. *Mater. Chem. Phys.* **2021**, *258*, 123888. [CrossRef]
24. Mohanty, D.; Satpathy, S.K.; Behera, B.; Mohapatra, R.K. Dielectric and frequency dependent transport properties in magnesium doped $CuFe_2O_4$ composite. *Mater. Today Proc.* **2020**, *33*, 5226–5231. [CrossRef]
25. Priyadharsini, R.; Das, S.; Venkateshwarlu, M.; Deenadayalan, K.; Manoharan, C. The influence of reaction and annealing temperature on physical and magnetic properties of $CuFe_2O_4$ nanoparticles: Hydrothermal method. *Inorg. Chem. Commun.* **2022**, *140*, 109406. [CrossRef]
26. Xu, P.; Xie, S.; Liu, X.; Wang, L.; Jia, X.; Yang, C. Electrochemical enhanced heterogenous activation of peroxymonosulfate using $CuFe_2O_4$ particle electrodes for the degradation of diclofenac. *Chem. Eng. J.* **2022**, *446*, 136941. [CrossRef]
27. Ge, Y.-C.; Wang, Z.-L.; Yi, M.-Z.; Ran, L.-P. Fabrication and magnetic transformation from paramagnetic to ferrimagnetic of $ZnFe_2O_4$ hollow spheres. *Trans. Nonferrous Met. Soc. China* **2019**, *29*, 1503–1509. [CrossRef]
28. Mohanty, D.; Mallick, P.; Biswall, S.K.; Behera, B.; Mohapatra, R.K.; Behera, A.; Satpathy, S.K. Investigation of structural, dielectric and electric properties of $ZnFe_2O_4$. *Mater. Today Proc.* **2020**, *33*, 4971–4975. [CrossRef]
29. Junlabhut, P.; Nuthongkum, P.; Pechrapa, W. Influences of calcination temperature on structural properties of $MnFe_2O_4$ nanopowders synthesized by co-precipitation method for reusable absorbent materials. *Mater. Today Proc.* **2018**, *5*, 13857–13864. [CrossRef]
30. Sivakumar, P.; Ramesh, R.; Ramanand, A.; Ponnusamy, S.; Muthamizhchelvan, C. Synthesis and characterization of $NiFe_2O_4$ nanoparticles and nanorods. *J. Alloys Compd.* **2013**, *563*, 6–11. [CrossRef]
31. Airimioaei, M.; Ciomaga, C.E.; Apostolescu, A.; Leonite, L.; Iordan, A.R.; Mitoseriu, L.; Palamaru, M.N. Synthesis and functional properties of the $Ni_{1-x}Mn_xFe_2O_4$ ferrites. *J. Alloys Compd.* **2011**, *509*, 8065–8072. [CrossRef]
32. Mathubala, G.; Manikandan, A.; Arul Antony, S.; Ramar, P. Photocatalytic degradation of methylene blue dye and magnetooptical studies of magnetically recyclable spinel $Ni_xMn_{1-x}Fe_2O_4$ ($x = 0.0 - 1.0$) nanoparticles. *J. Mol. Struct.* **2016**, *113*, 79–87. [CrossRef]
33. Dippong, T.; Levei, E.A.; Cadar, O. Formation, structure and magnetic properties of MFe_2O_4@SiO_2 (M = Co, Mn, Zn, Ni, Cu) nanocomposites. *Materials* **2021**, *14*, 1139. [CrossRef]
34. Alarifi, A.; Deraz, N.M.; Shaban, S. Structural, morphological and magnetic properties of $NiFe_2O_4$ nano-particles. *J. Alloy. Compd.* **2009**, *486*, 501–506. [CrossRef]
35. Naseri, M.G.; Bin Saion, E.; Ahangar, H.A.; Hashim, M.; Shaari, A.H. Synthesis and characterization of manganese ferrite nanoparticles by thermal treatment method. *J. Magn. Magn. Mater.* **2011**, *323*, 1745–1749. [CrossRef]
36. Joint Committee on Powder Diffraction Standards. *International Center for Diffraction Data*; ASTM: Philadelphia, PA, USA, 1999.

37. Ati, M.A.; Othaman, Z.; Samavati, A. Influence of cobalt on structural and magnetic properties of nickel ferrite nanoparticles. *J. Mol. Struct.* **2013**, *1052*, 177–182. [CrossRef]
38. Vinosha, P.A.; Xavier, B.; Krishnan, S.; Das, S.J. Investigation on zinc substituted highly porous improved catalytic activity of $NiFe_2O_4$ nanocrystal by co-precipitation method. *Mater. Res. Bull.* **2018**, *101*, 190–198. [CrossRef]
39. Jadhav, J.; Biswas, S.; Yadav, A.K.; Jha, S.N.; Bhattacharyya, D. Structural and magnetic properties of nanocrystalline Ni-Zn ferrites: In the context of cationic distribution. *J. Alloys Compd.* **2017**, *696*, 28–41. [CrossRef]
40. Salunkhe, A.B.; Khot, V.M.; Phadatare, M.R.; Thorat, N.D.; Joshi, R.S.; Yadav, H.M.; Pawar, S.H. Low temperature combustion synthesis and magnetostructural properties of Co-Mn nanoferrites. *J. Magn. Magn. Mater.* **2014**, *352*, 91–98. [CrossRef]
41. Lemine, O.M.; Bououdina, M.; Sajieddine, M.; Al-Saie, A.M.; Shafi, M.; Khatab, A.; Al-Hilali, M.; Henini, M. Synthesis, structural, magnetic and optical properties of nanocrystalline $ZnFe_2O_4$. *Phys. B* **2011**, *406*, 1989–1994. [CrossRef]
42. Yadav, S.P.; Shinde, S.S.; Bhatt, P.; Meena, S.S.; Rajpure, K.Y. Distribution of cations in $Co_{1-x}Mn_xFe_2O_4$ using XRD, magnetization and Mossbauer spectroscopy. *J. Alloys Compd.* **2015**, *646*, 550–556. [CrossRef]
43. Stefanescu, M.; Stoia, M.; Caizer, C.; Dippong, T.; Barvinschi, P. Preparation of $Co_xFe_{3-x}O_4$ nanoparticles by thermal decomposition of some organo-metallic precursors. *J. Therm. Anal. Calorim.* **2009**, *97*, 245–250. [CrossRef]
44. Sontu, U.B.; Yelasani, V.; Musugu, V.R.R. Structural, electrical and magnetic characteristics of nickel substituted cobalt ferrite nanoparticles, synthesized by self combustion method. *J. Magn. Magn. Mater.* **2015**, *374*, 376–380. [CrossRef]
45. Bameri, I.; Saffari, J.; Baniyaghoob, S.; Ekrami-Kakhki, M.S. Synthesis of magnetic nano-$NiFe_2O_4$ with the assistance of ultrasound and its application for photocatalytic degradation of Titan Yellow: Kinetic and isotherm studies. *Colloid Interface Sci. Commun.* **2022**, *48*, 100610. [CrossRef]
46. Belhadj, H.; Messaoudi, Y.; Khelladi, M.R.; Azizi, A. A facile synthesis of metal ferrites (MFe_2O_4, M = Co, Ni, Zn, Cu) as effective electrocatalysts toward electrochemical hydrogen evolution reaction. *Int. J. Hydrog. Energy* **2022**, *47*, 20129–20137. [CrossRef]